Astronomy & Astrophysics

VLT/UVES observations of extremely strong intervening damped Lyman-α systems

Molecular hydrogen and excited carbon, oxygen, and silicon at log N(H I) = 22.4[⋆]

P. Noterdaeme[1], R. Srianand[2], H. Rahmani[3,4], P. Petitjean[1], I. Pâris[5,6], C. Ledoux[7], N. Gupta[2], and S. López[5]

[1] Institut d'Astrophysique de Paris, CNRS-UPMC, UMR 7095, 98bis bd Arago, 75014 Paris, France
e-mail: noterdaeme@iap.fr
[2] Inter-University Centre for Astronomy and Astrophysics, Post Bag 4, Ganeshkhind, 411 007 Pune, India
[3] Institute for Research in Fundamental Sciences (IPM), PO Box 19395-5531, Tehran, Iran
[4] Laboratoire d'Astrophysique de Marseille, CNRS/Aix-Marseille Université, UMR 7326, 13388 Marseille, France
[5] Departamento de Astronomía, Universidad de Chile, Casilla 36-D, Santiago, Chile
[6] Osservatorio Astronomico di Trieste, via G. B. Tiepolo 11, 34131 Trieste, Italy
[7] European Southern Observatory, Alonso de Córdova 3107, Vitacura, Casilla 19001, Santiago 19, Chile

ABSTRACT

We present a detailed analysis of three extremely strong, intervening damped Lyman-α systems (ESDLAs, with log N(H I) $\geq$ 21.7) observed towards quasars with the Ultraviolet and Visual Echelle Spectrograph on the Very Large Telescope. We measure overall metallicities of [Zn/H] $\sim$ $-1.2, -1.3$, and -0.7 at, respectively, z_{abs} = 2.34 towards SDSS J214043.02−032139.2 (log N(H I) = 22.4 ± 0.1), z_{abs} = 3.35 towards SDSS J145646.48+160939.3 (log N(H I) = 21.7 ± 0.1), and z_{abs} = 2.25 towards SDSS J015445.22+193515.8 (log N(H I) = 21.75 ± 0.15). Iron depletion of about a factor 15 compared to volatile elements is seen in the DLA towards J2140−0321, while the other two show deletion that is typical of known DLAs. We detect H$_2$ towards J2140−0321 (log N(H$_2$) = 20.13 ± 0.07) and J1456+1609 (log N(H$_2$) = 17.10 ± 0.09) and argue for a tentative detection towards J0154+1935. Absorption from the excited fine-structure levels of O I, C I, and Si II are detected in the system towards J2140−0321, which has the largest H I column density detected so far in an intervening DLA. This is the first detection of O I fine-structure lines in a QSO-DLA, which also provides us with a rare possibility to study the chemical abundances of less abundant atoms like Co and Ge. Simple single-phase photo-ionisation models fail to reproduce all the observed quantities. Instead, we suggest that the cloud has a stratified structure: H$_2$ and C I most likely stem from a dense (log n_H $\sim$ 2.5−3) and cold (80 K) phase and from a warm (250 K) phase. They contain a fraction of the total H I, while a warmer (T > 1000 K) phase probably contributes significantly to the high excitation of O I fine-structure levels. The observed C I/H$_2$ column density ratio is surprisingly low compared to model predictions, and we do not detect CO molecules: this suggests a possible underabundance of C by 0.7 dex compared to other alpha elements. The absorber could be a photo-dissociation region close to a bright star (or a star cluster) where higher temperature occurs in the illuminated region. Direct detection of on-going star formation through e.g. near-infrared emission lines in the surroundings of the gas would enable a detailed physical modelling of the system.

Key words. quasars: absorption lines

1. Introduction

Diffuse gaseous clouds in the Universe are primarily described by their neutral hydrogen column density, which is a quantity that can be directly and accurately measured in absorption against background sources. The study of Ly α absorption lines in quasar spectra currently allows us to detect H I over ten orders of magnitude in column density, from N(H I) $\sim$ 10^{12} to 10^{22} cm^{-2}, and over a wide range of redshifts.

Several observations at low redshift show that clouds with log N(H I) > 15 tend to cluster around galaxies (e.g. Tripp et al. 1998; Bowen et al. 2002; Prochaska et al. 2011). In particular, Lyman-limit systems (LLS), with log N(H I) $\sim$ 17−18, are likely to trace cool circumgalactic environments, with a possible

bimodality in metallicity that would represent outflows of metal-rich gas and accretion of metal-poor gas by galaxies (Lehner et al. 2013). An inflexion in the H I column density distribution function is seen at log N(H I) $\sim$ 19, owing to the onset of self-shielding (Petitjean et al. 1992). When the column density reaches log N(H I) $\sim$ 20, the gas is mostly neutral and produces strong Ly α absorption with prominent Lorentzian wings. The corresponding absorbers are called damped Lyman-α systems (DLAs) when log N(H I) $\geq$ 20.3 (Wolfe et al. 1986). These systems are thought to arise when the line of sight passes a small impact parameter to a foreground galaxy. Early evidence of this came mostly from the similarity with H I column densities in nearby galactic discs and the presence of metals at different levels of chemical enrichment: the smoking gun of star-formation activity. Interestingly, this N(H I)-threshold also corresponds to the value above which Galactic gas clouds have a high fraction of cold neutral medium (Kanekar et al. 2011), a prerequisite for star formation. One can naively assume that the higher the

---

H I column density, the closer the association between the absorbing gas and a galaxy.

High redshift DLAs have been intensively studied (see Wolfe et al. 2005, for a review), with the main goal being to put constraints on the formation and evolution of galaxies in the early Universe, as well as to understand the links between star-formation activity and the distribution, physical, and chemical state of the gas. Systematic surveys for DLAs yielded a measurement of the cosmological density of neutral gas (e.g. Prochaska & Wolfe 2009; Noterdaeme et al. 2009b), which is a key ingredient for constraining hydrodynamical simulations of galaxy formation (Pontzen et al. 2008; Altay et al. 2013) and for understanding gas consumption by star formation, as well as feedback effects. Because metals are released in the interstellar medium (ISM) by the stars with different time scales, studies of both the overall metal abundances (e.g. Rao et al. 2005; Rafelski et al. 2012) and the abundance ratios (e.g. Petitjean et al. 2008; Pettini et al. 2008; Zafar et al. 2014) constrains the star-formation history. It is also possible to derive the physical state of the gas from the excitation of atomic and molecular species. In particular, the surrounding UV field can be estimated, thereby constraining the instantaneous star formation rates (SFRs), see e.g. Noterdaeme et al. (2007), Srianand et al. (2005), Wolfe et al. (2004). Overall, DLAs are a very important probe of various physical processes that are at play in the formation of galaxies (e.g. Bird et al. 2014).

A steepening of the N(H I)-frequency distribution at the very high column density end has long been discussed. It is possible that at least a fraction of high-column-density systems (in particular those with high metallicity) are missed in magnitude-limited QSO surveys (e.g. Boissé et al. 1998). However, radio-selected DLA samples appeared not to differ significantly from optically selected ones (e.g. Ellison et al. 2005; Jorgenson et al. 2006), at least in terms of H I-content. Another explanation, proposed by Schaye (2001), is that the high-column-density gas collapses into molecular hydrogen, eventually leading to star formation. Somehow paradoxically, this important mechanism at the heart of galaxy formation is observationally supported by the absence of high column densities, molecular gas and in situ star formation in DLA samples (see Krumholz et al. 2009). It is therefore important to directly search for these three ingredients and to study the relation between them.

Molecular gas has a very small covering fraction, making it unlikely to be found along a given random line of sight (Zwaan & Prochaska 2006). Nevertheless, efficient searches based on the presence of strong neutral carbon lines – which is an indicator of cold gas – have allowed us to detect translucent clouds for the first time (the regime inbetween diffuse and dense molecular clouds, see e.g. Snow & McCall 2006) in high-redshift DLAs (Srianand et al. 2008; Noterdaeme et al. 2009a, 2010, 2011). While the N(H I)-distribution of C I-selected absorbers is found to be flatter than for regular DLAs (i.e. H I-selected), the former population is still dominated by low N(H I), and the current sample (66 C I systems, Ledoux et al. 2015) does not contain very large H I column densities. The strong reddening by these systems also reinstates the possibility of a dust bias against the cold phase. Finally, C I systems frequently present the 2175 Å absorption feature, although with a reduced strength compared to Milky Way lines of sight, possibly because of strong UV field originating from in situ star formation.

The detection of very high column density DLAs is possible through searching large datasets of quasar spectra. Using the Sloan Digital Sky Survey (SDSS, York et al. 2000), Noterdaeme et al. (2009b) showed that the slope of the N(H I) distribution at the high end is actually shallower than previously thought, with

the first detection of a QSO-DLA reaching log N(H I) = 22 (in which H_2 is detected, Guimarães et al. 2012). The tremendous increase of available quasar spectra (Pâris et al. 2012, 2014) in the SDSS-III Baryon Oscillation Spectroscopic Survey (BOSS, Dawson et al. 2013) allowed to extend the study to even higher column densities (Noterdaeme et al. 2012b), with a slope similar to what is seen from opacity-corrected 21-cm maps in the local Universe (Braun 2012). The analysis of stacked spectra showed that extremely strong DLAs (ESDLAs, with log N(H I) $\geq$ 21.7) are likely to arise from galaxies at small impact parameters (b < a few kpc) with average star formation rates of the order of 2 $M_\odot$ yr^{-1} (Noterdaeme et al. 2014). X-shooter observations of a system with log N(H I) = 22.10 towards the quasar SDSS J113520.39−001053.5 resulted in the detection of a star-forming galaxy at b < 1 kpc from the quasar line of sight (Noterdaeme et al. 2012a; see also Kulkarni et al. 2012), making it possible the first mass determination of a DLA galaxy by weak lensing (Grillo & Fynbo 2014).

Here, we search for molecular hydrogen in extremely strong DLAs, using high-resolution spectroscopic observations. We present the observations and data reduction in Sect. 2 and the abundance measurements in Sect. 3. We then investigate the chemical and physical conditions in the highest N(H I) QSO-DLA detected so far in Sect. 4. We summarise and conclude in Sect. 5.

2. Observations and data reduction

The three quasars were observed in service mode with the Ultraviolet and Visual Echelle Spectrograph (UVES, Dekker et al. 2000) mounted on the Very Large Telescope UT2 of the European Southern Observatory under Programme ID 091.A-0370(A). The total 15 600 s of science exposure of each object was divided into four exposures of 3900 s each. All observations of SDSS J214043.02−032139.2 (z_{em} = 2.48, hereafter J2140−0321) and SDSS J015445.22+193515.8 (z_{em} = 2.53, hereafter J0154+1935) were performed using the standard beam splitter in 390+580 setting that covers roughly from 330 to 450 nm on the blue CCD, and from 465 to 578 nm and 583 to 680 nm on the two red CCDs. Observations of SDSS J145646.48+160939.3 (z_{em} = 3.68, hereafter J1456+1609) included three exposures using the 390+760 setting that roughly covers wavelength ranges of 567 to 754 nm and 763 to 946 nm for the two red CCDs along with an exposure in 390+580 setting. The slit width of 1 arcsec and a CCD readout with 2 × 2 binning used for all the observations resulted in a spectral resolution power $R \approx$ 48 000 dispersed on pixels of ~2.0 km s^{-1}. The log of the observations is provided in Table 1.

We reduced the raw frames to extract the 1D spectra using the UVES Common Pipeline Library (CPL) data reduction pipeline release 6.3[1] by implementing the optimal extraction. Polynomials of 4th order were used to find the wavelength solution and the rms calibration error was found to be always less than 100 m s^{-1}. We shifted the individual science exposures to the heliocentric-vacuum frame correcting for the observatory's motion towards the line of sight at the exposure mid point and using the air-to-vacuum relation from Ciddor (1996). We then re-binned individual spectra to a common wavelength array, scaled and combined them altogether using weights estimated from the errors in each pixel while rejecting bad pixels and cosmic-ray impacts at the same time. In the following, abundances

---

[1] http://www.eso.org/sci/facilities/paranal/instruments/uves/doc/

Table 1. Log of VLT/UVES observations.

QSO	Observing dates	Setting	Exposure time	Seeing (″)	Airmass
SDSS J214043.02−032139.2	15-06-2013/02-07-2013	390+580	4×3900 s	0.7−0.8	1.1
SDSS J145646.48+160939.3	06-05-2013/12-05-2013	390+760	3×3900 s	0.9	1.3−1.4
	07-06-2013	390+580	1×3900 s	1.0	1.3
SDSS J015445.22+193515.8	01-09-2013/04-09-2013/05-09-2013	390+580	4×3900 s	0.8−1.0	1.4
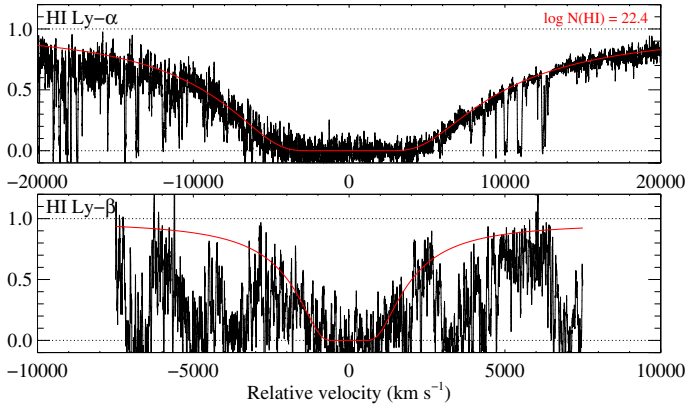
Fig. 1. Voigt-profile fitting to the damped Ly α (*top*) and Ly β (*bottom*) lines at $z_{\rm abs} = 2.34$ towards J2140−0321. The normalised spectrum has been boxcar-smoothed by 10 pixels only for presentation. We note that here, and in all figures representing Voigt-profile fits to the data, the y-axis corresponds to the normalised flux (unitless).

are expressed relative to solar, i.e. $[{\rm X/H}] \equiv \log N({\rm X})/N({\rm H}) - \log({\rm X/H})_\odot$, where we adopted the solar abundances of Asplund et al. (2009).

3. Abundance measurements

3.1. Neutral hydrogen

The DLA at $z_{\rm abs} = 2.34$ towards J2140−0321 presents a very wide dark core and extended wings that decrease the quasar continuum over several hundred angstroms. Noterdaeme et al. (2014) used a principal component analysis (see Pâris et al. 2011) on the low-resolution, flux-calibrated BOSS spectrum to get a first estimate of the unabsorbed quasar continuum, including the Ly α emission line. They derived $\log N({\rm H\,I}) = 22.35$ by fitting the damped Ly α line. Fitting both the damped Ly α and Ly β absorption lines in the UVES spectrum together with the quasar continuum, we derive $\log N({\rm H\,I}) = 22.40 \pm 0.10$, see Fig. 1. This represents the highest column density ever found in a high-z intervening cloud.

Similarly, we derive the H I column densities in the DLAs at $z_{\rm abs} = 3.35$ towards J1456+1609 (Fig. 2) and $z_{\rm abs} = 2.155$ towards J0154+1935 (Fig. 3). For J1456+1609, we use the Ly α, Ly β and Ly γ to constrain the fit while only Ly α is covered with sufficient signal-to-noise ratio (S/N) for J0154+1935. We obtain $\log N({\rm H\,I}) = 21.70 \pm 0.10$ and 21.75 ± 0.15, respectively. These values are also in good agreement with the respective values of $\log N({\rm H\,I}) = 21.85$ and 21.77 derived from the BOSS data.

3.2. Metallicity and dust depletion

We analyse the three spectra using standard χ^2-minimisation of multiple Voigt-profiles performed with vpfit v9.5[2]. The velocity profiles of the metals and the corresponding best Voigt-profile

---

[2] Carswell http://www.ast.cam.ac.uk/~rfc/vpfit.html
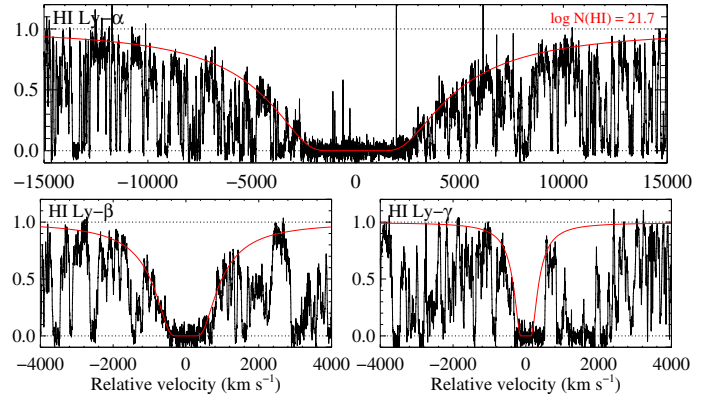
Fig. 2. Same as Fig. 1 for the DLA towards J1456+1609. Boxcar-smoothed by 5 pixels only for presentation.
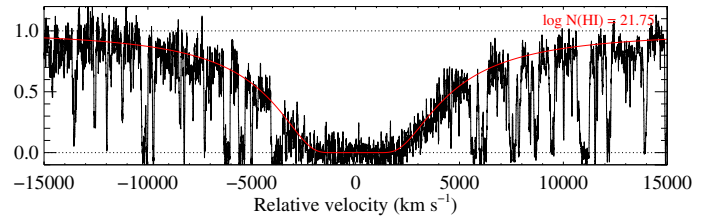

Fig. 3. Same as Fig. 1 for the DLA towards J0154+1935. Boxcar-smoothed by 10 pixels only for presentation.

fitting are shown in Fig. 4. For the three systems, the metal profiles are rather compact and the decomposition into individual components is not unique. Therefore, we quote the total column densities in Table 2, i.e. summed over all velocity components, which should in principle be more reliable and depend less on the exact velocity component decomposition. We also independently checked our results using the apparent optical depth method (AOD, see Savage & Sembach 1991; Fox et al. 2005). The weighted-mean values obtained by applying this technique to several unblended transitions are in very good agreement with those based on Voigt-profile fitting.

Since Zn II is a volatile species, it is expected to be undepleted onto dust grains and to be one of the best indicator of the true metallicity. We do not apply any ionisation correction, which should actually be very small given the very large H I column densities in the clouds (see e.g. Péroux et al. 2007).

The metallicity measurement is particularly difficult for the system towards J2140−0321: a two-component model with $\log N({\rm Zn\,II}) \sim 13.4$ provides a good fit to the bulk of the profile. However, Zn II λ2026 is very strong and unfortunately the only zinc line covered by our spectrum. This makes the column density highly uncertain, despite a satisfactory fit. A more careful look at the metal profile, in particular Ni II lines, reveals a central narrow component. We find a fitting solution that converges with a very narrow component ($b \sim 1.2$ km s^{-1}) that contains a significant amount of Zn II: we then get a total $\log N({\rm Zn\,II}) \sim 13.7$, i.e. a factor of two higher than above.
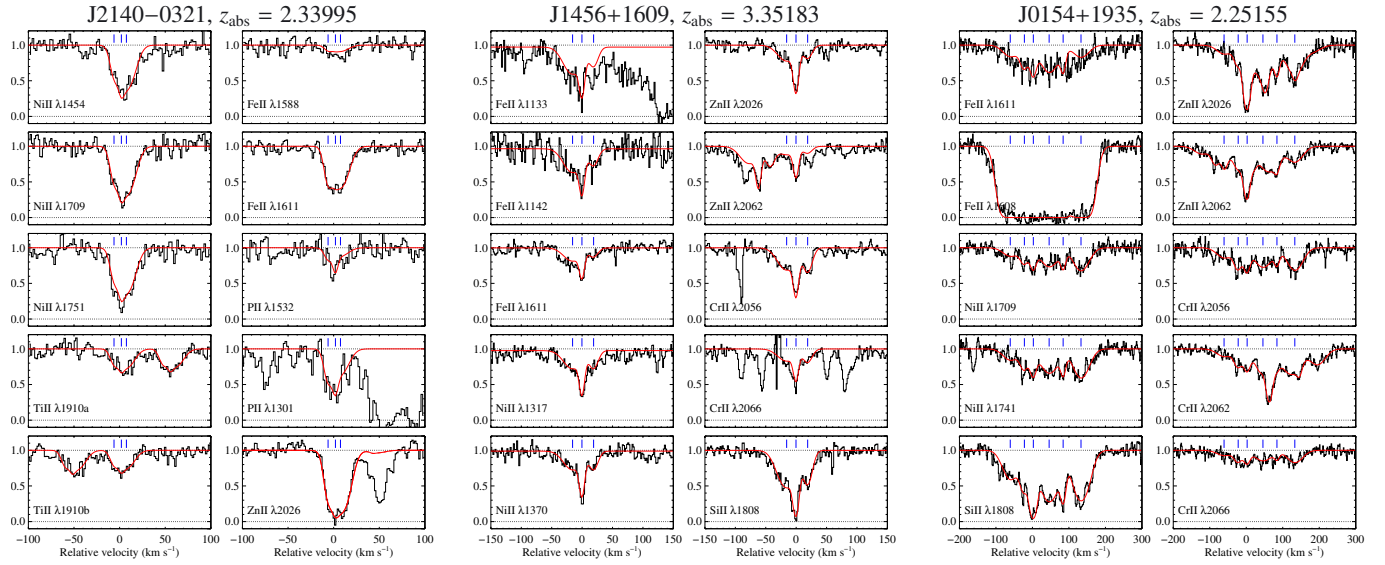
Fig. 4. Voigt-profile fit to the metal absorption lines in the three ESDLAs. The redshift that defines the origin of the velocity scale, indicated on the top, corresponds to that of the cold gas (from C I for J2140−0321, J0154+1935 and from H₂ for J1456+1609). The blue ticks indicate the position of the individual velocity components in the fit.

Table 2. Overall column densities and abundances.

Species	$\log N$ [cm^{-2}]		
	J2140−0321, $z_{abs} = 2.34$	J1456+1609, $z_{abs} = 3.35$	J0154+1935, $z_{abs} = 2.25$
H I	22.40 ± 0.10	21.70 ± 0.10	21.75 ± 0.15
Si II	…	15.81 ± 0.05 (15.83)	16.42 ± 0.02
	…	[Si/H] = −1.40 ± 0.11	[Si/H] = −0.84 ± 0.15
P II	14.76 ± 0.08 (14.74)	…	…
	[P/H] = −1.05 ± 0.13	…	…
Ti II	13.26 ± 0.05 (13.27)	…	…
	[Ti/H] = −2.09 ± 0.11	…	…
Cr II	…	13.75 ± 0.04 (13.68)	14.07 ± 0.01 (14.09)
	…	[Cr/H] = −2.22 ± 0.11	[Cr/H] = −1.32 ± 0.15
Fe II	15.64 ± 0.03 (15.60)	15.39 ± 0.06 (15.44)	16.09 ± 0.02 (16.13)
	[Fe/H] = −2.26 ± 0.10	[Fe/H] = −1.81 ± 0.12	[Fe/H] = −1.16 ± 0.15
Ni II	14.40 ± 0.05 (14.36)	14.09 ± 0.03 (14.11)	14.62 ± 0.02 (14.67)
	[Ni/H] = −2.22 ± 0.11	[Ni/H] = −1.83 ± 0.10	[Ni/H] = −1.35 ± 0.15
Zn II	13.72 ± 0.92	12.94 ± 0.04 (12.87)	13.66 ± 0.02 (13.75)
	[Zn/H] = −1.24 ± 0.93	[Zn/H] = −1.32 ± 0.11	[Zn/H] = −0.65 ± 0.15

Notes. Column densities derived from the apparent optical depth method are indicated in parenthesis (see text). Abundances are expressed with respect to photospheric solar values from Asplund et al. (2009).

The uncertainty on the Zn II column density becomes also much larger and we get [Zn/H] ∼ −1.24±0.93. Unfortunately the AOD method cannot be used to derive N(Zn II) from Zn IIλ2026 because the flux in this line reaches zero values. A higher resolution spectrum covering also Zn IIλ2062 is therefore required to get a more precise abundance of zinc. Our spectrum covers the position of P IIλλ1301,1532 that are fortunately not saturated, and from which we derive [P/H] ∼ −1.05. Because phosphorus is likely a non-refractory element (see e.g. Molaro et al. 2001, and references therein), we can use it as an indicator of the metallicity for this system. For the DLAs towards J1456+1609 and J0154+1935, we find overall metallicities of respectively [Zn/H] = −1.3 and −0.7 based on unsaturated Zn IIλ2026 and Zn IIλ2062 absorption lines.

Ti II, Cr II, Ni II and Fe II are refractory elements that deplete easily onto dust grains (e.g. Pettini et al. 1997). We observe iron depleted by a factor about 15, 3 and 3 compared to non-depleted elements (Zn, P) in the systems towards respectively, J2140−0321, J1456+1609 and J0154+1935. The depletion patterns (Fig. 5) for the systems towards J1456+1609 and J0154+1935 are similar to that derived from stacking BOSS spectra of ESDLAs (Noterdaeme et al. 2014). This is typical of what is seen in the Small Magellanic Cloud (Welty et al. 1997), which also presents high H I column densities and relatively low metallicities. In turn, the depletion pattern in the DLA towards J2140−0321 is more similar to that seen in the warm ISM in the Milky-Way disc.

3.3. Molecular hydrogen

Molecular hydrogen absorption lines are unambiguously detected in the systems towards J2140−0321 and J1456+1609 from the Lyman ($B^1\Sigma_u^+ \leftarrow X^1\Sigma_g^+$) and/or Werner ($C^1\Pi_u \leftarrow X^1\Sigma_g^+$) electronic bands. In the former case, very strong Lyman-band
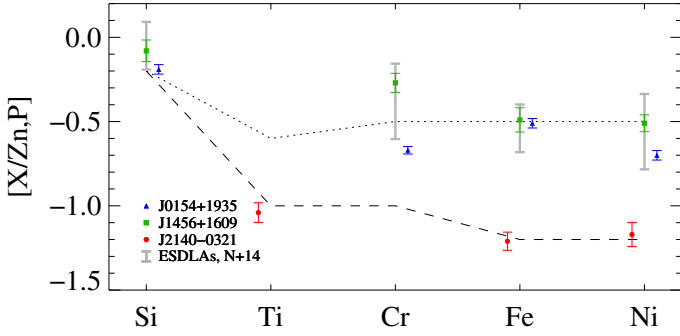
Fig. 5. Depletion patterns of different elements. For J2140−0321 we use the phosphorus abundance (relative to solar) as a proxy for that of zinc. The grey bars correspond to the value obtained from averaging low-resolution BOSS spectra of ESDLAs (Noterdaeme et al. 2014). The dotted (resp. dashed) line corresponds to the Milky-Way halo (resp. warm disc) depletion pattern.

Table 3. Molecular hydrogen in the z_{abs} = 2.34 DLA towards J2140−0321.

H$_2$ Rot. level	z_{abs}	b [km s^{-1}]	log N [cm^{-2}]
$J = 0$	2.33990	–	19.84 ± 0.09
$J = 1$	2.33999	–	19.81 ± 0.04
$J = 2$	2.33997	4.0 ± 0.7	17.96 ± 0.14
$J = 3$	2.33997	4.9 ± 0.7	17.76 ± 0.40
$J = 4$	2.33996	6.5 ± 0.5	15.88 ± 0.26
$J = 5$	2.33998	5.7 ± 1.8	15.17 ± 0.16
$J = 6$	2.33998		≤14.72
Total			20.13 ± 0.07
			log $f = -1.97 \pm 0.17$

absorptions are seen up to rotational level $J = 5$ (Fig. 6), with damping wings for the first two rotational levels in all transitions and for several $J = 2$ lines. This allows for accurate column density measurements in these low rotational levels. In turn, all $J = 3$ lines are on the flat part of the curve of growth, implying a higher measurement uncertainty. Some $J \geq 4$ lines are unsaturated, making again the column density measurement in principle more reliable. We note that the H$_2$ absorption is well modelled by a single component but with slightly different Doppler parameters and redshifts for the different rotational levels. This indicates that the different rotational populations of H$_2$ may not be fully co-spatial with a possible velocity structure in the H$_2$ gas that is not resolved into distinct components with the current data. The column densities in the individual rotational levels of H$_2$ are provided in Table 3. We measure a total H$_2$ column density of log N(H$_2$) = 20.13 ± 0.07, from which we derive the overall molecular fraction log $f = -2.14 \pm 0.17$, where $f = 2N(\text{H}_2)/(2N(\text{H}_2) + N(\text{H I}))$.

H$_2$ lines are much weaker towards J1456+1609, but still detected in a single component up to $J = 4$ thanks to the large oscillator strengths of the lines in the covered Lyman and Werner bands (Fig. 7 and Table 4). We measure log N(H$_2$) = 17.10 ± 0.09, which corresponds to log $f = -4.30 \pm 0.20$. Since the errors in each rotational level are not independent, the total error is taken from the extremum values in each level.

Unfortunately, the S/N of our UVES spectrum of J0154+1935 is too low in the blue to firmly detect H$_2$. This makes any χ^2-minimisation unreliable as the total χ^2 changes little irrespective of the assumed column density. Rebinning the UVES spectrum by 4 pixels (Fig. 8), we can see however that the

Table 4. Molecular hydrogen in the z_{abs} = 3.35 DLA towards J1456+1609.

H$_2$ Rot. level	z_{abs}	b [km s^{-1}]	log N [cm^{-2}]
$J = 0$	3.351829	0.6 ± 0.1	16.09 ± 0.26
$J = 1$	''		16.75 ± 0.05
$J = 2$	''		16.29 ± 0.10
$J = 3$	''		16.49 ± 0.06
$J = 4$	''		15.78 ± 0.16
Total	''		17.10 ± 0.09
			log $f = -4.30 \pm 0.20$

Table 5. Neutral carbon in the z_{abs} = 2.25 DLA towards J0154+1935.

C I fine-structure level	z_{abs}	log N [cm^{-2}]	b [km s^{-1}]
$J = 0$ (g.s.)	2.25152	13.39 ± 0.06	5.2 ± 0.7
	2.25163	13.06 ± 0.21	6.3 ± 2.0
$J = 1$ (*)	2.25152	13.47 ± 0.06	5.2 ± 0.7
	2.25163	13.19 ± 0.14	6.3 ± 2.0
$J = 2$ (**)	2.25152	12.71 ± 0.10	5.2 ± 0.7
	2.25163	12.56 ± 0.21	6.3 ± 2.0
Total		13.95 ± 0.05	

data is consistent with the presence of H$_2$ with column density in the range log N(H$_2$) = 17−19, assuming a thermal excitation of T = 100 K and a Doppler parameter b = 3 km s^{-1}, typical of what is seen in other H$_2$ absorbers. Neutral carbon absorption lines, in turn, are unambiguously detected in two components in this system, with N(C I) $\simeq 10^{14}$ cm^{-2}, see Fig. 9 and Table 5. Given the first ionisation potential of carbon (11.2 eV), the presence of strong C I absorption is a reliable indicator of the presence of H$_2$ in the cloud (Srianand et al. 2005).

4. The DLA towards J2140−0321: chemical and physical conditions

In this section, we study the z_{abs} = 2.34 system towards J2140−0321 in more details, as it is particularly interesting for having the largest H I and H$_2$ column densities ever measured in a high-z QSO-DLA. In addition, the presence of chlorine, as well as fine-structure lines of C I, O I and Si II allows us to probe the chemical and physical conditions prevailing in the absorbing gas as well as the multicomponent nature of the absorber. In particular, we apply standard procedures used in Galactic ISM studies to extract physical parameters like density, temperature and radiation field and compare them with those derived for the H$_2$ clouds in different environments. We also consider photo-ionisation models using the code CLOUDY to confirm our findings.

4.1. Heavy elements

Different elements are released by stars through several channels, depending on the stellar masses and life-times. The very high column densities towards J2140−0321 provide a unique opportunity to detect rare heavy elements, bringing additional clues to the chemical enrichment history of the cloud.

Absorption lines from Ge II and Co II are probably detected in our spectrum, albeit at less than 3σ significance level and from single lines (Fig. 10). We estimate the corresponding column densities to be log N(Ge II) $\sim$ 12.25 and log N(Co II) $\sim$ 13.05
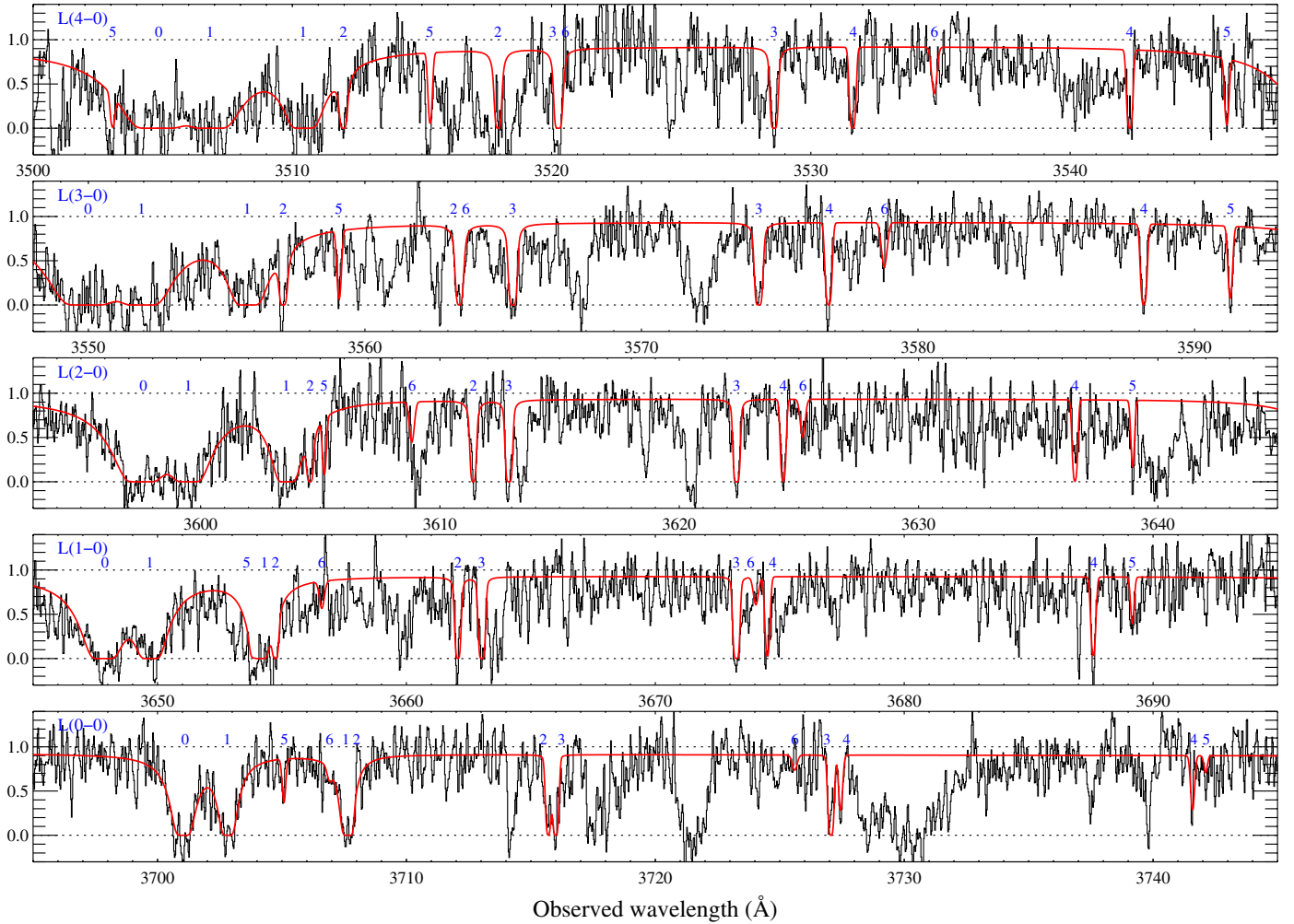
Fig. 6. Portions of the UVES spectrum of J2140−0321 covering H_2 absorption lines at z_{abs} = 2.34. The data has been boxcar-smoothed by 3 pixels only for the sake of visual clarity. Each wavelength region covers a Lyman band, indicated in the top left corner of each panel. The numbers in blue above each absorption line indicate the rotational level to which the line belongs.

from fitting these lines with the redshifts and Doppler parameters fixed to those derived from the other metals. We then derive [Ge/H] ∼ −1.8 and [Co/H] ∼ −2.3. Germanium is the heaviest element detected in our spectrum, and has very rarely been detected in DLAs to date (Prochaska et al. 2003; Dessauges-Zavadsky et al. 2006). Measuring the abundance of germanium is of particular interest because its nucleosynthesis resides at the transition between explosive synthesis of iron-peak elements and neutron-capture synthesis of heavier elements. In metal-poor stars, the abundance of germanium seems to follow well that of iron (Cowan et al. 2005), favouring an explosive origin of this element at low metallicity, while the increase of [Ge/Fe] with metallicity (Roederer 2012) indicates the onset of *s*-process production of germanium at high metallicity. Here, the observed ratio is super-solar ([Ge/Fe] ∼ 0.46), similar to what is seen in other DLAs (Dessauges-Zavadsky et al. 2006). However, iron is a refractory element that very easily depletes onto dust grains, making it difficult to interpret the observed ratio in terms of nucleosynthesis. Unfortunately, the abundance of undepleted elements zinc and sulphur are not well constrained in the DLA towards J2140−0321 while Ni is also depleted. A possible reference element could be phosphorus, which seems to be little depleted. However, its exact nucleosynthesis is still not fully understood (Molaro et al. 2001). The observed sub-solar [Ge/P]

ratio ([Ge/P] ∼ −0.75) could partly be due to depletion of germanium but could also reflect an enrichment dominated by massive stars. Cobalt is also rarely seen in DLAs, with the first detection reported by Ellison et al. (2001). As argued by these authors, the similar depletion of cobalt and iron should make the [Co/Fe] ratio little dependent on the actual amount of dust. Here, we measure a solar cobalt-to-iron ratio, similar to what is seen in the DLA towards Q 0948+43 (Rao et al. 2005), and in the Galactic disc (e.g. Prochaska et al. 2000). The DLA towards J2140−0321 therefore appears to be an excellent place to study the nucleosynthesis processes at the origin of the chemical enrichment, although further observations, with higher S/N, better wavelength coverage (in particular for Cu II that falls in a gap of our spectrum and for Zn II, for which only one transition is covered) and higher spectral resolution are required to put strong constraint on the abundances.

4.2. Neutral chlorine

Chlorine is a peculiar species whose ionisation potential (12.97 eV) should make Cl II its dominant form in atomic gas. However, in the presence of H_2, chemical reactions make Cl I the dominant form of chlorine (Jura 1974): Cl^0 results from the
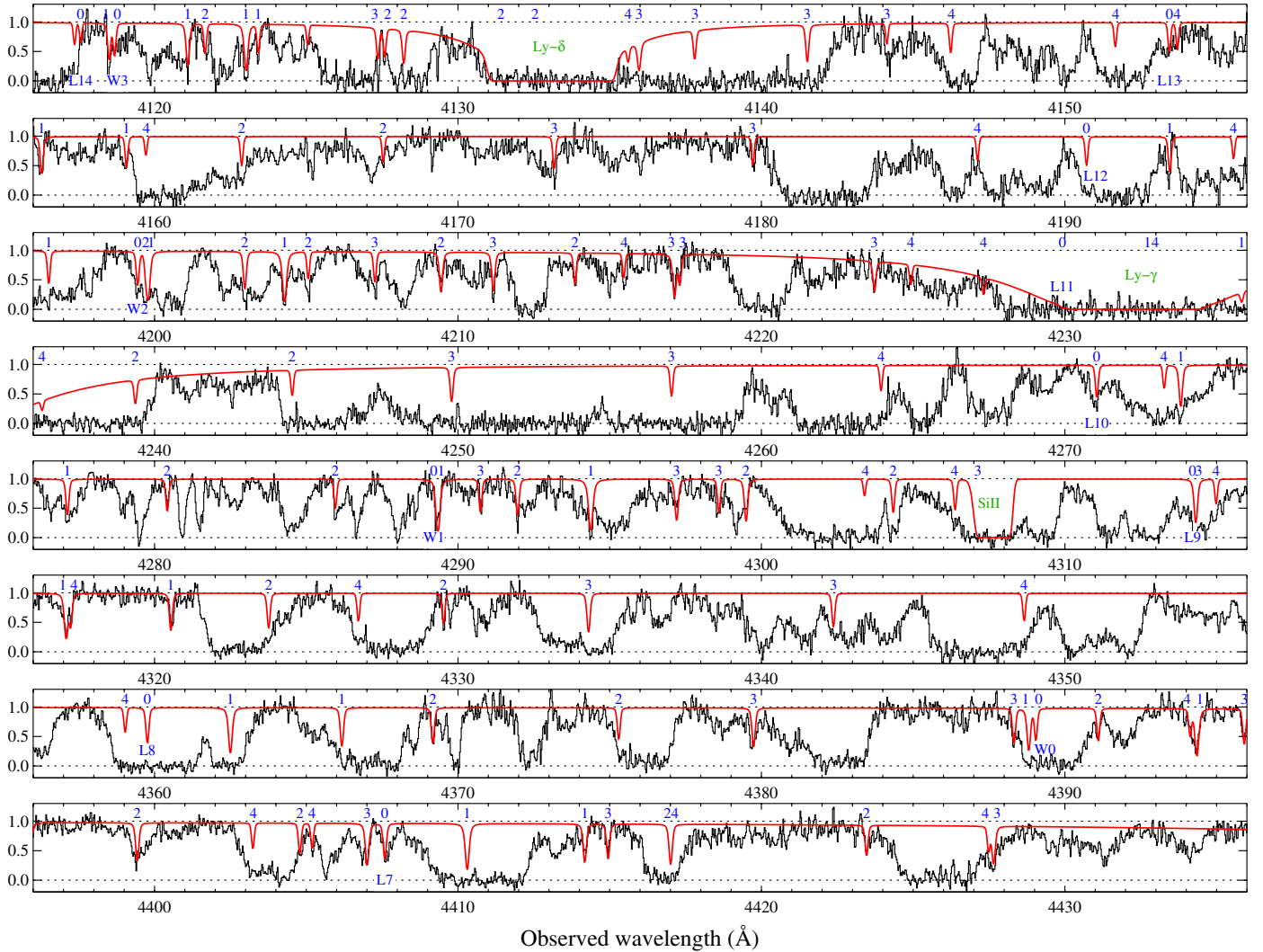
Fig. 7. Portion of the J1456+1609 spectrum covering H_2 absorption lines at z_{abs} = 3.35. The number in blue above each line corresponds to its rotational level. The Lyman and Werner bands are indicated as blue label below each J = 0 H_2 line. Other absorption lines from the same system are labelled in green (Ly γ Ly δ and Si II).

exothermic reaction $Cl^+ + H_2 \rightarrow HCl^+$ that has a very high rate (Fehsenfeld & Ferguson 1974). Several channels then allow the quick release of Cl I, in particular from collisions with H_2 or electrons.

In addition, Cl I is little depleted onto dust grains and should be an excellent tracer of clouds with high molecular fractions (e.g. Jura & York 1978; Sonnentrucker et al. 2002; Balashev et al. 2015). Cl I has been detected in the translucent cloud at z_{abs} = 2.7 towards the quasar SDSS J1237+0647 (Noterdaeme et al. 2010), that has high molecular fraction f_{H2} > 0.3 and also harbours CO molecules. Here, we detect a strong Cl Iλ1347 line (see Fig. 11), from which we derive log N(Cl I) = 13.61 ± 0.10 cm^{-2} when all parameters are left free. However, the data is noisy and that b may be overestimated. Since Cl I is expected to be related to the cold gas phase, we rather expect a velocity broadening more similar to that of H_2 (or C I) and a good velocity match between these species. We therefore perform a second fit, fixing b to 5 km s^{-1}. This gives log N(Cl I) = 13.69 ± 0.13 cm^{-2}. We therefore adopt the value log N(Cl I) = 13.67 ± 0.15, where the error conservatively represent the full range allowed by the two fits and their associated uncertainties. Because Cl I is little depleted into dust and arises in the H_2-bearing gas, its column density can provide a rough idea of the amount of H I present

in that cold gas, provided its metallicity is known. Assuming a value equal to the overall metallicity, we estimate that the H_2-bearing gas contains a few times 10^{21} cm^{-2} of the total hydrogen column density ($10^{22.4}$ cm^{-2}). The molecular fraction in the remaining gas is likely too low to make chemical reactions with H_2 counterbalance the Cl I photoionisation rate.

4.3. Carbon monoxide

We do not detect CO absorption lines. In order to get a stringent limit, we stacked the covered CO AX absorption bands (from (0−0) to (3−0)), weighting each band by f/σ_c^2, where f is the oscillator strength and σ_c the noise in the continuum. This way, the S/N in the stack is maximised[3]. We assume an excitation temperature corresponding to radiative equilibrium with the cosmic microwave background, as seen in high-z CO absorption systems (Noterdaeme et al. 2011) and derive N(CO) < 5 × 10^{13} cm^{-2}, see Fig. 12. This corresponds to CO/H_2 ~ 0.4 × 10^{-6}, more than an order of magnitude less than what has been measured in CO-bearing DLAs (Srianand et al. 2008; Noterdaeme et al. 2010), but consistent with the ratio observed towards Galactic

---

[3] The signal here refers to the amplitude of the absorption, not the continuum.
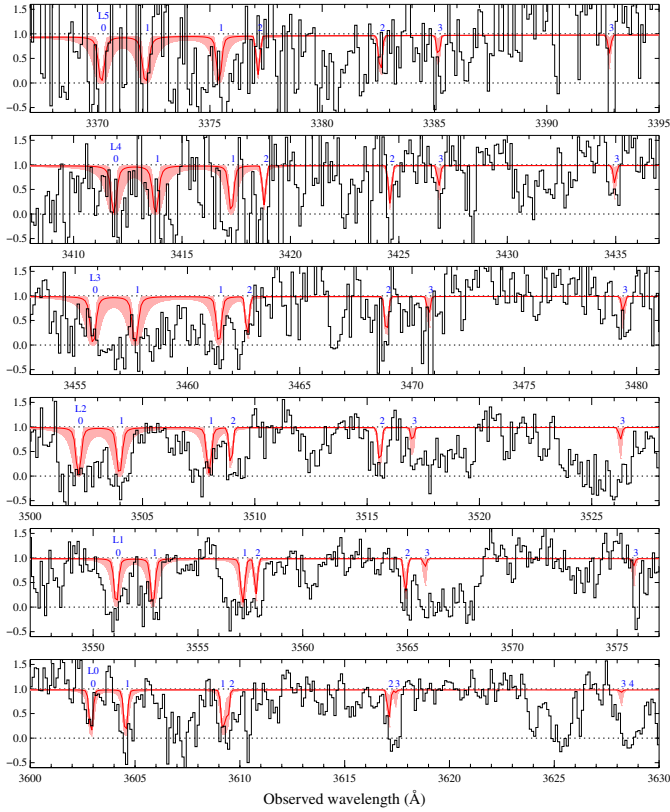
Fig. 8. Portion of the UVES spectrum of J0154+1935 covering the location of Lyman-bands of H_2 (from L(0−0) to L(5−0)). The spectrum has been rebinned by 4 pixel. The red synthetic profile corresponds to $N(H_2) = 10^{18}$ cm^{-2} with a single excitation temperature of 100 K. The shaded region corresponds to ±1 dex range in $N(H_2)$ around this column density.
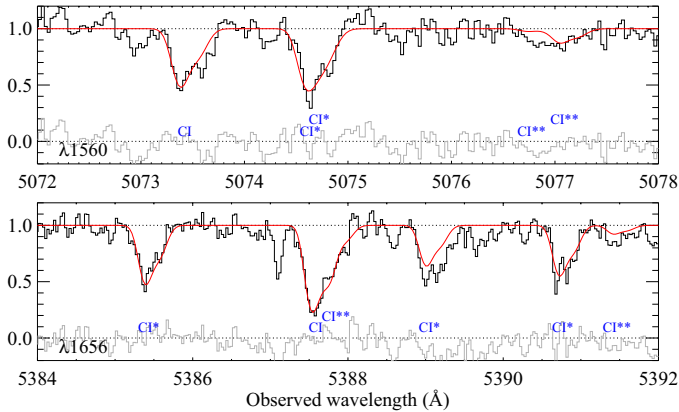

**Fig. 9.** C I absorption lines in the $z_{abs} = 2.25$ DLA towards J0154+1935.

stars with the same H_2 column density (e.g. Fig. 4 of Burgh et al. 2007). This shows that high H_2 column density is not a sufficient condition for the presence of CO (see also Bolatto et al. 2013).

### 4.4. Excitation of H_2: gas kinetic temperature and UV pumping

At log $N(H_2) \geq 16$, the low rotational level populations are most likely to be in thermal equilibrium. Therefore, the corresponding excitation temperature provides a good estimate of the gas
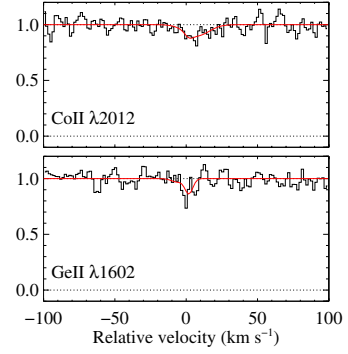
Fig. 10. Possible detection of Co II and Ge II in the DLA towards J2140−0321.
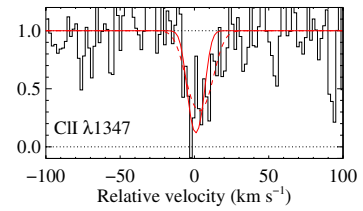
Fig. 11. Neutral chlorine in the DLA at $z_{abs} = 2.34$ towards J2140−0321. The dashed profile corresponds to a fit will all parameters free, while b is fixed to that of C I for the solid profile.
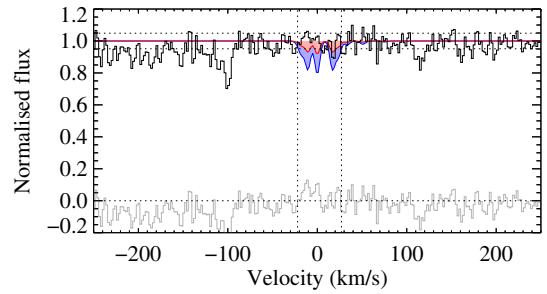

Fig. 12. Stack of covered CO AX absorption bands (from (0−0) to (3−0)) towards J2140. The red (resp. blue) profiles correspond to the expected profile having 1 time (resp. 3 times) the area sustained by noise (horizontal dotted lines) over the velocity range covered by the band (vertical lines) and assuming $T_{ex} = T_{CMB}$.

kinetic temperature (e.g. Roy et al. 2006; Le Petit et al. 2006). In Fig. 13, we show the population of the different rotational levels of H_2 as a function of the energy in these levels. The $J = 0$ to $J = 2$ levels can be explained by a single excitation temperature of $T_{ex} \sim 75$ K, which is lower than what is generally observed in both high-z and low-z H_2-bearing DLAs ($\langle T_{01} \rangle \sim 150$ K, Srianand et al. 2005; Muzahid et al. 2015) or at high Galactic latitude ($\langle T_{01} \rangle \sim 125$ K, Gillmon et al. 2006) but very similar to what is observed in the Galactic disc or in the Magellanic clouds ($T_{01} \sim 80$ K, Savage et al. 1977; Tumlinson et al. 2002; Welty et al. 2012).

The higher excitation temperature ($T_{ex} \sim 240$ K) inferred for $J \geq 3$ rotational levels shows that they are not thermalised if arising from the same region and that an additional excitation process is at play. Generally, such a situation is considered to be due to UV pumping, although H_2-formation on dust grains could contribute to populate the high energy levels (Wagenblast 1992). Another possibility could be that the high-J levels are also populated by collisional excitation, but in a warmer, presumably external layer of the cloud. The observed excitation
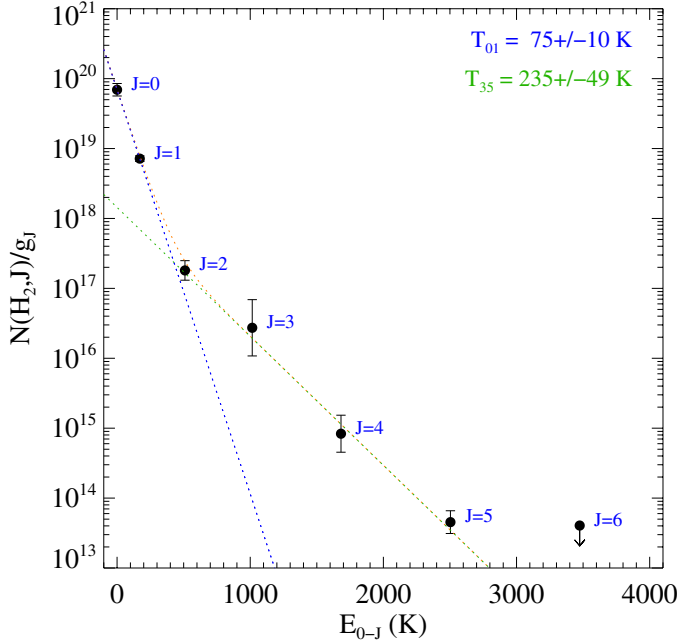
Fig. 13. Excitation diagram of H_2 towards J2140−0321. The straight blue (resp. green) dotted line corresponds to the excitation of the low (resp. high) rotational levels. The orange curve correspond to the sum of the two populations in Boltzmann equilibrium at the two different temperatures.

diagram would then be the sum of a low temperature component (having a temperature of ∼75 K), contributing to most of the low-J column density and a warmer component (having a temperature of ∼240 K), responsible for the high-J column densities. If we assume such an excitation temperature of the warm gas then the measured column densities at $J = 4$ and $J = 5$ are consistent with a total $\log N(H_2) \sim 19$ in this component.

4.5. Neutral carbon: volumic density of hydrogen and electrons in the cold phase

Absorption lines from neutral carbon in the ground state ($J = 0$, C I), first ($J = 1$, C I*) and second ($J = 2$, C I**) excited levels are detected in our spectrum (Fig. 14). From fitting the absorption lines around 1560 and 1656 Å (in the DLA's rest-frame), that are located outside the Ly α-forest, we derive the total (ground and excited states) C I column density to be $\log N(\text{C I}) = 13.57 \pm 0.03$. Both the C I*/C I and C I**/C I ratios indicate high particle density in the cloud. From Fig. 2 of Silva & Viegas (2002) and Fig. 12 of Srianand et al. (2005), we can already see that the density in the C I-bearing gas should be of the order of $n_H \sim 200\,\text{cm}^{-3}$. We note that at such density, the contribution from radiative excitation (UV pumping and cosmic microwave background) becomes negligible compared to collisions. While C I and H_2 are not necessarily fully co-spatial, to the first order, we can consider this density to be that of the molecular gas. We note that this implies that the cloud is of pc-scale, when considering about 10% of H I in this phase (Sects. 4.3 and 4.9).

For the inferred metallicity, if we ignore the depletion of C into dust grains and a possible under-abundance of carbon compared to other elements, we expect $N(\text{C II}) \simeq 6 \times 10^{17}\,\text{cm}^{-2}$. This implies $N(\text{C I})/N(\text{C II}) = 10^{-4.2}$. Using Eq. (5) of Srianand et al. (2005) we derive $n_e/\Gamma = 1.4 \times 10^6$ when we assume $T \sim 100$ K. Here, Γ is the photo-ionisation rate of C^0. If we
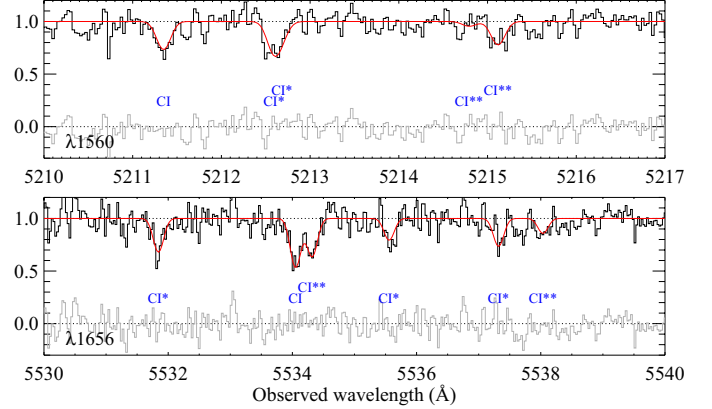
Fig. 14. Neutral carbon in the DLA at $z_{abs} = 2.34$ towards J2140−0321.

Table 6. Additional species at $z_{abs} = 2.34$ towards J2140−0321.

| Species	$\log N$ [cm^{-2}]	b [km s^{-1}]
C I, $J = 0$ (g.s)	13.03 ± 0.04	5.0 ± 0.8
C I, $J = 1$ (*)	13.20 ± 0.04	''
C I, $J = 2$ (**)	13.02 ± 0.05	''
total	13.57 ± 0.03	
Cl I	13.67 ± 0.15	$5-10^a$
CO	<13.73	
O I, $J = 2$ (g.s.)	$17.9^{\,b}$	11
O I, $J = 1$ (*)	13.89 ± 0.11	9.5 ± 1.0^c
O I, $J = 0$ (**)	13.85 ± 0.08	9.5 ± 1.0
Si II, $J = 1/2$ (g.s.)	≥ 16.16	
Si II, $J = 3/2$ (*)	12.81 ± 0.03	9.5 ± 0.8

Notes. $^{(a)}$ The two values correspond to b fixed to that of C I and that obtained when left as free parameter. $^{(b)}$ Value from fitting the line, consistent with the [Zn/H] and [P/H] ratios. See text. $^{(c)}$ Because O I*λ1304 is noisy, we fixed b to the value obtained from fitting O I**λ1306 alone.

take $\Gamma \sim 2 \times 10^{-10}$ found in our galaxy (Welty et al. 2003) then we get $n_e \simeq 3 \times 10^{-4}$. This value is much lower than the inferred range $(0.7-4.7) \times 10^{-2}$ in other high-z H_2 absorbers using similar approach (see Table 4 of Srianand et al. 2005). We note however that the lower inferred electron density could also result from a much higher actual photo-ionisation rate than the Galactic mean value or the inferred $\log N(\text{C II})$ is overestimated. Indeed, carbon could actually be under-abundant, similarly to what has been suggested for the lack of C I in a low-z H_2 DLA (Srianand et al. 2014). We will come back to this while discussing photo-ionisation models.

4.6. Fine-structure levels of O I

We detect very strong O Iλ1302 absorption together with the absorption from the two fine-structure levels of the ground state (O I*λ1304 and O I**λ1306, see Fig. 15)^4. This is, to our knowledge, the first detection of excited neutral oxygen in an intervening absorption system. However, O I* and O I** are more commonly detected in DLAs associated to GRB afterglows (Vreeswijk et al. 2004; Chen et al. 2005; Fynbo et al. 2006), where it is generally interpreted as an indicator of high volumic density. Unfortunately, the weaker O Iλ1355 line is not covered

---

^{4} Note that the ground state of neutral oxygen is comprised of the $2s^2 2p^4\ ^3P^e_{J=2,1,0}$ fine-structure levels, the ground-state of which correspond to $J = 2$.
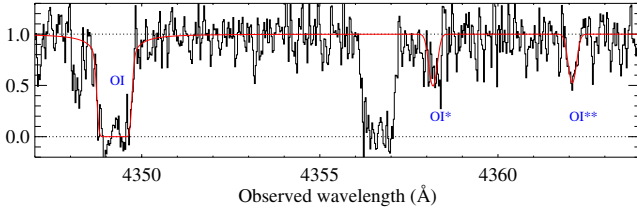
Fig. 15. Neutral oxygen fine-structure lines in the DLA at z_{abs} = 2.34 towards J2140−0321. The absorption lines seen at $\lambda \approx 4348$ and 4356.5 Å correspond to P IIλ1301 and Si IIλ1304, respectively.

by our spectrum and other O I lines are far in the blue and strongly blended in the Ly α forest. Fitting the O Iλ1302 absorption line with a single component gives $\log N(\text{O I}) = 17.9 \pm 0.2$. The Doppler parameter is left free and we find $b \simeq 11$ km s^{-1}, surprisingly close to the $b \sim 12$ km s^{-1} expected from the velocity width of the profile ($\Delta_v \simeq 28$ km s^{-1}, Sect. 4.8), using the relation between these quantities from Noterdaeme et al. (2014). The derived oxygen abundance would then be [O/H] ~ -1.2, i.e. consistent with that derived from zinc and phosphorus.

We derive $\log N(\text{O I}^*) = 13.89 \pm 0.11$ and $\log N(\text{O I}^{**}) = 13.85 \pm 0.07$ from fitting O I$^*\lambda$1304 and O I$^{**}\lambda$1306. We note however that the former line is noisy and possibly affected by blends. We therefore fixed the Doppler parameter to the value from O I$^{**}\lambda$1306 alone but note that this has little influence on the derived column density.

Using the H I collisional rate constant from Abrahamsson et al. (2007) and radiative decay rates from Galavis et al. (1997), Jenkins & Tripp (2011) have found that $N(\text{O I}^*)/N(\text{O I}^{**})$ can be a good indicator of local kinetic temperature (see their Fig. 15). For $T \sim 80$ K as suggested by T_{01} we expect the ratio to be higher than 2. However, the observed ratio ($\sim$1) is rather consistent with a gas temperature of 1000 K. It is clear from Fig. 6 of Silva & Viegas (2002) that the observed ratio of $N(\text{O I}^*)/N(\text{O I})$ and $N(\text{O I}^{**})/N(\text{O I})$ cannot be reproduced by a single density for $T = 150$ K. However, this ratio can be reproduced for $T = 1000$ K and $n_H \sim 300$ cm^{-3}. It is also clear from Fig. 6 of Silva & Viegas (2002) that the UV pumping may not be very efficient for the observed range in ratios of column densities. Therefore, the observed fine-structure level populations of O I favours the presence of warm neutral gas in addition to the dense cold gas probed by the low rotational level population of H$_2$. Direct excitation by infra-red photons is also a possibility.

4.7. Excited C II and Si II

Strong and saturated C II$^*\lambda$1335 absorption is detected in this system, with an equivalent width of roughly 0.2 Å. Because the C II* column density is directly related to the gas cooling through C II 158 μm emission ($^2P_{3/2}$ (C II*) → $^2P_{1/2}$ (C II)), it allows in principle to derive the surrounding UV flux by equating this cooling rate with the heating from photo-electric effect onto dust grains (Wolfe et al. 2003), although cosmic-ray heating may contribute significantly as well (Dutta et al. 2014). Unfortunately, the strong saturation of C II$^*\lambda$1335 prevents meaningful measurement or useful limit on $N(\text{C II}^*)$ and the weaker C II$^*\lambda$1037 is blended with Ly α forest absorption. Nonetheless, the very strong absorption should still indicate significant cooling and hence star-formation activity.

The excited fine-structure level of ionised silicon (Si II($J = 3/2$) or Si II*) is also detected in this system. The first detection of this kind in an intervening system was reported by Kulkarni et al. (2012) in the extremely strong DLA
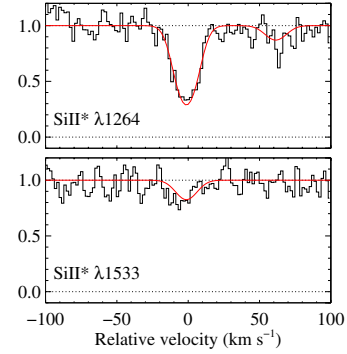
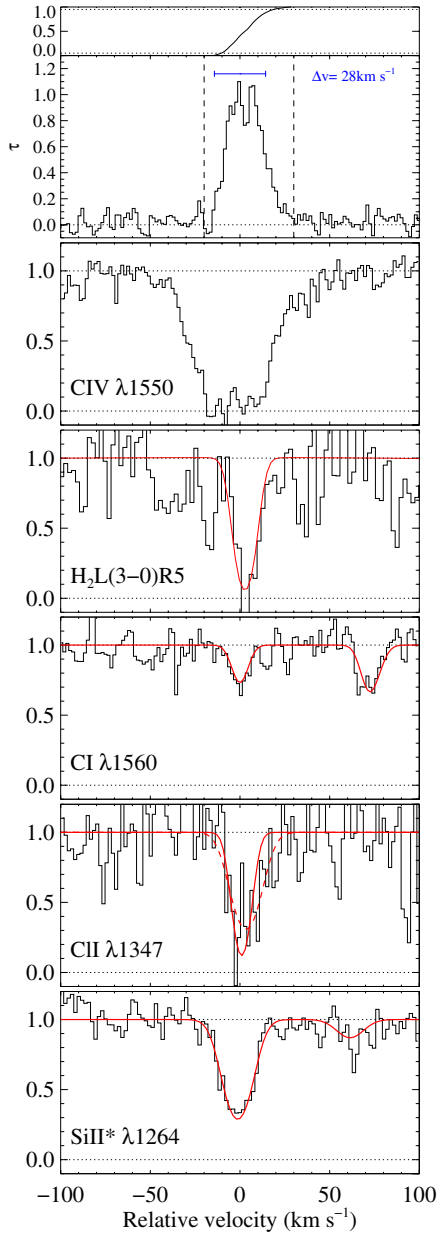**Fig. 16.** Si II* at z_{abs} = 2.34 towards J2140−0321. The absorption at +50 km s^{-1} in the Si II$^*\lambda$1264 panel is due to Si II$^*\lambda$1265.

towards J1135−0010, which arises from a young low-impact parameter galaxy with $SFR \sim 25\,M_\odot$ yr^{-1} (Noterdaeme et al. 2012a). More recently, Neeleman et al. (2015) suggested that this line arises from highly turbulent ISM in young star-forming galaxies. Here, we unambiguously detect Si II$^*\lambda$1264, Si II$^*\lambda$1265 and Si II$^*\lambda$1533 (Fig. 16) from which we derive $\log N(\text{Si II}^*) = 12.81 \pm 0.03$. Assuming an intrinsic solar abundance ratio of silicon with respect to zinc and 0.2 dex depletion onto dust as seen in different galactic and DLA environments (Fig. 5), we estimate, in the gas phase, $N(\text{Si II})$ to be about a few times 10^{16} cm^{-2}, implying $N(\text{Si II}^*)/N(\text{Si II}) \sim 10^{-4}$. It is well known that the electron collisional cross-section is three orders of magnitude higher than that of hydrogen for the fine-structure excitation of Si II. If we consider only the collisions by electrons followed by radiative de-excitation we get $n_e \sim 0.8$ cm^{-3} if Si II* absorption is associated to the H$_2$ gas with $T \sim 100$ K (see Srianand & Petitjean 2000). We get $n_e \sim 0.06$ cm^{-3} if we assume the gas temperature to be 1000 K.

4.8. Kinematics

The study of the velocity extent of different species can provide an additional view of the overall puzzle (Fig. 17). The top panel presents the measurement of the velocity width defined as the interval comprised between 5% and 95% of the total optical depth of a low-ionisation species. We find $\delta v = 28$ km s^{-1}, which is in the low range of the distribution for the overall population of DLAs. This may be indicative of a low-mass system (Ledoux et al. 2006). The width[5] of the C IV profile ($FWHM \sim 40$ km s^{-1}) is also among the lowest measured in DLAs (Fox et al. 2007). This suggests a quiet environment: its origin could be due to photo-ionisation by nearby massive stars rather than collisional ionisation in a hot halo or in galactic winds (e.g. Oppenheimer & Davé 2006). We may anticipate that in situ star formation could contribute to the high excitation of Si II and O I. These excited species also have $b \sim 10$ km s^{-1}, twice larger than what is seen in the cold phase ($b(\text{C I}) \sim 5$ km s^{-1}), hence possibly arising from a warmer and more turbulent gas. In conclusion, we are likely observing cold gas in a star-forming region of a possibly low-mass galaxy. The presence of nearby massive stars would result in warming and exciting the outer layers of the cloud, giving rise to the observed Si II* and O I*.

---

[5] Because C IV is saturated, the kinematics cannot be quantified using the 5−95% range of the optical depth.

Fig. 17. Measurement of metal-absorption kinematics (using Fe IIλ1611, *top panel*) at z_{abs} = 2.34 towards J2140−0321. The *other panels* represent the normalised spectrum around several species on the same velocity scale.

4.9. Comparisons with models

In this section, we intent to understand the abundances and excitation of the different species in a single picture by comparing the observations with models using the spectral simulation code CLOUDY (Ferland et al. 1998), including the micro-physics of H_2 (Shaw et al. 2005).

To start with, we consider the case of absorbing gas not associated to any star-forming region. In this case we assume the ionising radiation to be the meta-galactic UV background dominated by QSOs and Galaxies (see for example Haardt & Madau 2012). We assume the metallicity and dust depletion to be identical to the observed values. For simplicity we assume the gas temperature to be 80 K as inferred from T_{01} and did not ask the code to self-consistently obtain this temperature. The calculations are stopped when the total H_2 column density in

the model reaches the observed value. We run the model for a range of hydrogen densities. These "cold" models correspond to the solid black lines in Fig. 18. We find that the observed abundance of chlorine in the cold gas can be reproduced for $1.4 \leq \log n_H \leq 1.8$. However, this density range is inconsistent with the C I fine-structure excitation and the density is also too low to explain the high excitation of oxygen fine-structure levels. Conversely, a higher density model ($\log n_H \sim 2.7$), consistent with the C I fine-structure excitation under-predicts the abundance of chlorine. This happens because H_2 is then formed more efficiently and reaches the observed column density at a much lower total gas column. Finally, we note that the predicted C I column density in the cold phase is about a factor 20 above the observed values.

Therefore, we considered another set of models where we also include the local radiation field. For this we considered the Galactic UV background given by Habing (1968) scaled by χ. For simplicity, we also scale the cosmic ray density by the same amount. We considered $\chi = 1, 10$ and 30 (respectively dotted, dashed and dash-dotted curves). We also consider a set of model with the addition of a warmer component ($T \sim 300$ K) that contains $\log N(H_2) \sim 19$, as discussed in Sect. 4.4. These models ("cold+warm") are shown as orange curves in Fig. 18.

We can see that irrespective of the radiation field and the inclusion or not of a warm envelope, the fine-structure excitation of C I indicates a high density as derived above. The inclusion of a warm phase makes the different ratios in better agreement with each other, although C I** tends require slightly higher excitation than C I*. As we already consider excitation by cosmic microwave background, collisions and UV pumping self-consistently in CLOUDY, the additional pumping could be related to local infra-red radiation field not explicitly included in our models. However, if we allow for 1.5σ uncertainties in the measured ratios then our models can consistently reproduce the observations when $2.5 \leq \log n_H \leq 3.0$. For this range in density the observed $N(Cl\,I)$ requires χ close to or slightly below 10. In that case, the cold phase should contain between 10% and 50% of the total hydrogen column density while these values are between 30% and 80% when adding the warmer phase.

The addition of the warm phase improves significantly the agreement between the predicted and observed ratio of O I fine-structure levels, in particular the O I*/O I ratio. In turn, Si II*/Si II becomes now over-predicted for the above χ and n while the changes are still not good enough to explain the high O I**/O I* ratio. In the case of silicon, we remind that we were unable to measure $N(Si\,II)$ directly due to line saturation, so the disagreement remains reasonable. We also note that a lower density in the warm phase ($\log n \sim 2$) than in the cold phase would help making the agreement between model and observations better. Indeed, as noted before from Fig. 6 of Silva & Viegas (2002), it is clear that when $T = 150$ K (close to what we use in our models) the very similar value of 10^{-4} found for $N(O\,I^*)/N(O\,I)$ and $N(O\,I^{**})/N(O\,I)$ cannot be produced by a single density. In turn, from the bottom panels of the same figure we can see it will be easier to find a solution when the gas temperature is 1000 K. Therefore, it is also possible that the fine-structure excitation of O I originates from an even warmer (i.e. $\geq$1000 K) phase than the one probed by H_2 absorption, presumably with a lower density. This phase would not contribute to the observed Cl I column density but would contain the remaining H I.

However, the addition of an even warmer phase without H_2 that could explain O I* and O I** will not solve the problem with C I. Also, as can be seen from the corresponding panel in Fig. 18, increasing further the ionisation rate of carbon is not an option
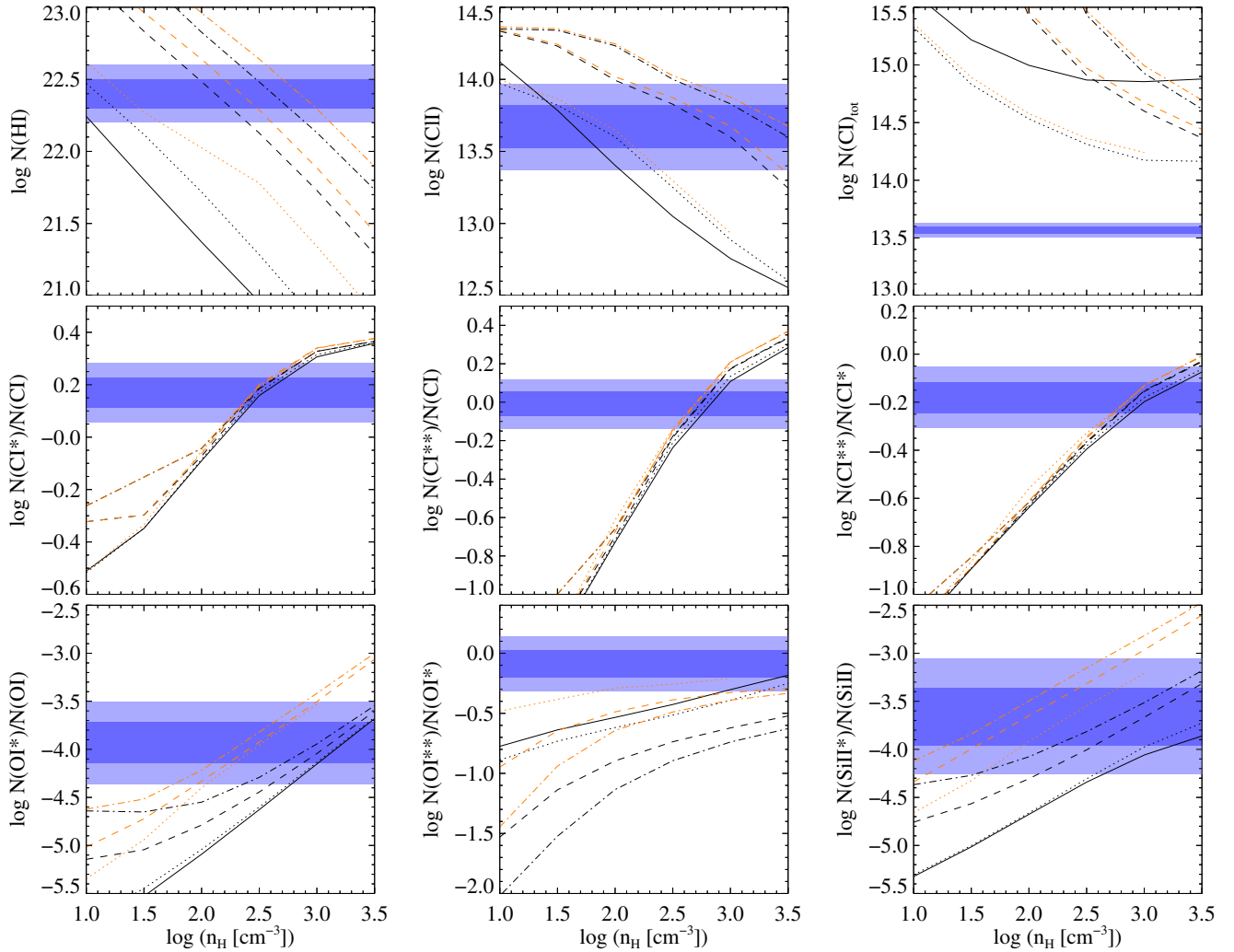
Fig. 18. Results of photo-ionisation models. For each hydrogen density the calculation is stopped when the observed $N(H_2)$ is reached. The blue shaded regions give the 1 and 2σ range on the *total* column density (*top*) or column density ratios (*bottom*) from the observations. The solid, dotted, dashed and dashed-dotted lines correspond to an in situ radiation field of respectively $\chi = 0, 1, 10, 30$ times the local Galactic field. The cold-gas-only model ($T = 80$ K, $\log N(H_2) = 20.13$) is represented by black lines while the orange lines represent the model with an additional warm component ($T = 300$ K and $\log N(H_2) = 19$).

as it also alters the H_2 equilibrium. Reducing the recombination rate can be achieved by reducing the electron density that will not alter the H_2 equilibrium abundance. Because H I is self-shielded, the electron density in the H_2 gas will originate from the photo-ionisation of metals, grains and primary and secondary ionisation by cosmic rays. Grain recombination also controls the electron density. One important step towards understanding this issue is to measure $N(C\,II)$ accurately. The expected value suggests that C IIλ1334 should have detectable damping wings. Unfortunately, the S/N of our spectrum is still too low to firmly detect the damping wings and constrain $N(C\,II)$. Another (simpler) possibility is that the gas phase abundance of carbon is much lower than assumed. Assuming 0.4 dex depletion of C onto dust grains as seen in the cold ISM, the true abundance of carbon in the DLA should be of the order of [C/O] ~ -0.7 or even less for the gas phase column density to be consistent with the models. This is indeed similar to what is seen in Milky-way halo stars with metallicity similar to the present DLA (Akerman et al. 2004). In addition, while [C/H] is difficult to measure in DLAs, available measurements towards very low metallicity DLAs do not rule out this possibility (Cooke et al. 2011; Dutta et al. 2014).

5. Conclusion

We have presented high resolution spectroscopic observations of three ESDLAs with $\log N(H\,I) \geq 21.7$. We have firmly detected H_2 in two of them, towards J2140−0321 and J1456+1609. H_2 is also likely present with a high column density in the third system, towards J0154+1935, but additional data is required to firmly establish this. This recommends a systematic survey for H_2 in EDLAs as the H_2 detection rate may be much higher even though the measured overall molecular fractions are not as high as those expected in translucent and dense molecular regions.

We studied in details the system towards J2140−0321, which has the highest H I and H_2 column densities observed till now in a high-z intervening system ($\log N(H\,I) = 22.4$) and presents several excited fine-structure transitions that help constraining the physical conditions. Cobalt and germanium are likely detected in our spectrum, although more data would be required to use these species to constraint accurately the nucleosynthesis history of this DLA. The abundance and excitation of different species shows that H_2 is predominantly originating from a cold dense phase ($T \sim 80$ K, $\log n_H \sim 2.5-3$) where chlorine is found in neutral form due to chemical reactions with H_2.

However, models indicate that the addition of warmer phases is required to better explain the high excitation of oxygen and silicon, consistently with the wider velocity profile of these species. Nevertheless, even considering multiple phases, all models overproduce C I, if we assume a solar abundance of carbon with respect to other elements. This may in turn indicate that the [C/O] ratio is actually much lower than solar in this DLA, similarly to what has been seen in Milky-Way halo stars. We conclude that the absorbing gas is likely made of multiple phases having temperature in the range 80 to 1000 K irradiated by an local radiation field due to in situ star formation. This is also consistent with the picture that extremely strong DLAs arise at very small impact parameters from star-forming galaxies (Noterdaeme et al. 2014), i.e. likely arise from their disc or inner regions.

Finally, direct detection of star-formation activity through the detection of near-infrared emission lines should bring invaluable clues to complete the picture: it should allow us to better understand the excitation of the absorbing gas and link its properties with the overall properties of the DLA galaxy.

References

Abrahamsson, E., Krems, R. V., & Dalgarno, A. 2007, ApJ, 654, 1171
Akerman, C. J., Carigi, L., Nissen, P. E., Pettini, M., & Asplund, M. 2004, A&A, 414, 931
Altay, G., Theuns, T., Schaye, J., Booth, C. M., & Dalla Vecchia, C. 2013, MNRAS, 436, 2689
Asplund, M., Grevesse, N., Sauval, A. J., & Scott, P. 2009, ARA&A, 47, 481
Balashev, S. A., Noterdaeme, P., Klimenko, V. V., et al. 2015, A&A, 575, L8
Bird, S., Vogelsberger, M., Haehnelt, M., et al. 2014, MNRAS, 445, 2313
Boissé, P., Le Brun, V., Bergeron, J., & Deharveng, J.-M. 1998, A&A, 333, 841
Bolatto, A. D., Wolfire, M., & Leroy, A. K. 2013, ARA&A, 51, 207
Bowen, D. V., Pettini, M., & Blades, J. C. 2002, ApJ, 580, 169
Braun, R. 2012, ApJ, 749, 87
Burgh, E. B., France, K., & McCandliss, S. R. 2007, ApJ, 658, 446
Chen, H.-W., Prochaska, J. X., Bloom, J. S., & Thompson, I. B. 2005, ApJ, 634, L25
Ciddor, P. E. 1996, Appl. Opt., 35, 1566
Cooke, R., Pettini, M., Steidel, C. C., Rudie, G. C., & Nissen, P. E. 2011, MNRAS, 417, 1534
Cowan, J. J., Sneden, C., Beers, T. C., et al. 2005, ApJ, 627, 238
Dawson, K. S., Schlegel, D. J., Ahn, C. P., et al. 2013, AJ, 145, 10
Dekker, H., D'Odorico, S., Kaufer, A., Delabre, B., & Kotzlowski, H. 2000, in Optical and IR Telescope Instrumentation and Detectors, eds. M. Iye, & A. F. Moorwood, Proc. SPIE, 4008, 534
Dessauges-Zavadsky, M., Prochaska, J. X., D'Odorico, S., Calura, F., & Matteucci, F. 2006, A&A, 445, 93
Dutta, R., Srianand, R., Rahmani, H., et al. 2014, MNRAS, 440, 307
Ellison, S. L., Ryan, S. G., & Prochaska, J. X. 2001, MNRAS, 326, 628
Ellison, S. L., Hall, P. B., & Lira, P. 2005, AJ, 130, 1345
Fehsenfeld, F. C., & Ferguson, E. E. 1974, J. Chem. Phys., 60, 5132
Ferland, G. J., Korista, K. T., Verner, D. A., et al. 1998, PASP, 110, 761
Fox, A. J., Savage, B. D., & Wakker, B. P. 2005, AJ, 130, 2418
Fox, A. J., Ledoux, C., Petitjean, P., & Srianand, R. 2007, A&A, 473, 791
Fynbo, J. P. U., Starling, R. L. C., Ledoux, C., et al. 2006, A&A, 451, L47
Galavis, M. E., Mendoza, C., & Zeippen, C. J. 1997, A&AS, 123, 159
Gillmon, K., Shull, J. M., Tumlinson, J., & Danforth, C. 2006, ApJ, 636, 891
Grillo, C., & Fynbo, J. P. U. 2014, MNRAS, 439, L100
Guimarães, R., Noterdaeme, P., Petitjean, P., et al. 2012, AJ, 143, 147
Haardt, F., & Madau, P. 2012, ApJ, 746, 125
Habing, H. J. 1968, Bull. Astron. Inst. Netherlands, 19, 421
Jenkins, E. B., & Tripp, T. M. 2011, ApJ, 734, 65
Jorgenson, R. A., Wolfe, A. M., Prochaska, J. X., et al. 2006, ApJ, 646, 730
Jura, M. 1974, ApJ, 190, L33
Jura, M., & York, D. G. 1978, ApJ, 219, 861
Kanekar, N., Braun, R., & Roy, N. 2011, ApJ, 737, L33
Krumholz, M. R., Ellison, S. L., Prochaska, J. X., & Tumlinson, J. 2009, ApJ, 701, L12
Kulkarni, V. P., Meiring, J., Som, D., et al. 2012, ApJ, 749, 176
Le Petit, F., Nehmé, C., Le Bourlot, J., & Roueff, E. 2006, ApJS, 164, 506
Ledoux, C., Petitjean, P., Fynbo, J. P. U., Møller, P., & Srianand, R. 2006, A&A, 457, 71
Ledoux, C., Noterdaeme, P., Petitjean, P., & Srianand, R. 2015, A&A, accepted
Lehner, N., Howk, J. C., Tripp, T. M., et al. 2013, ApJ, 770, 138
Molaro, P., Levshakov, S. A., D'Odorico, S., Bonifacio, P., & Centurión, M. 2001, ApJ, 549, 90
Muzahid, S., Srianand, R., & Charlton, J. 2015, MNRAS, 448, 2840
Neeleman, M., Prochaska, J. X., & Wolfe, A. M. 2015, ApJ, 800, 7
Noterdaeme, P., Petitjean, P., Srianand, R., Ledoux, C., & Le Petit, F. 2007, A&A, 469, 425
Noterdaeme, P., Ledoux, C., Srianand, R., Petitjean, P., & Lopez, S. 2009a, A&A, 503, 765
Noterdaeme, P., Petitjean, P., Ledoux, C., & Srianand, R. 2009b, A&A, 505, 1087
Noterdaeme, P., Petitjean, P., Ledoux, C., et al. 2010, A&A, 523, A80
Noterdaeme, P., Petitjean, P., Srianand, R., Ledoux, C., & López, S. 2011, A&A, 526, L7
Noterdaeme, P., Laursen, P., Petitjean, P., et al. 2012a, A&A, 540, A63
Noterdaeme, P., Petitjean, P., Carithers, W. C., et al. 2012b, A&A, 547, L1
Noterdaeme, P., Petitjean, P., Pâris, I., et al. 2014, A&A, 566, A24
Oppenheimer, B. D., & Davé, R. 2006, MNRAS, 373, 1265
Pâris, I., Petitjean, P., Rollinde, E., et al. 2011, A&A, 530, A50
Pâris, I., Petitjean, P., Aubourg, É., et al. 2012, A&A, 548, A66
Pâris, I., Petitjean, P., Aubourg, É., et al. 2014, A&A, 563, A54
Péroux, C., Dessauges-Zavadsky, M., D'Odorico, S., Kim, T.-S., & McMahon, R. G. 2007, MNRAS, 382, 177
Petitjean, P., Bergeron, J., & Puget, J. L. 1992, A&A, 265, 375
Petitjean, P., Ledoux, C., & Srianand, R. 2008, A&A, 480, 349
Pettini, M., Smith, L. J., King, D. L., & Hunstead, R. W. 1997, ApJ, 486, 665
Pettini, M., Zych, B. J., Murphy, M. T., Lewis, A., & Steidel, C. C. 2008, MNRAS, 391, 1499
Pontzen, A., Governato, F., Pettini, M., et al. 2008, MNRAS, 390, 1349
Prochaska, J. X., & Wolfe, A. M. 2009, ApJ, 696, 1543
Prochaska, J. X., Naumov, S. O., Carney, B. W., McWilliam, A., & Wolfe, A. M. 2000, AJ, 120, 2513
Prochaska, J. X., Gawiser, E., Wolfe, A. M., Cooke, J., & Gelino, D. 2003, ApJS, 147, 227
Prochaska, J. X., Weiner, B., Chen, H.-W., Mulchaey, J., & Cooksey, K. 2011, ApJ, 740, 91
Rafelski, M., Wolfe, A. M., Prochaska, J. X., Neeleman, M., & Mendez, A. J. 2012, ApJ, 755, 89
Rao, S. M., Prochaska, J. X., Howk, J. C., & Wolfe, A. M. 2005, AJ, 129, 9
Roederer, I. U. 2012, ApJ, 756, 36
Roy, N., Chengalur, J. N., & Srianand, R. 2006, MNRAS, 365, L1
Savage, B. D., & Sembach, K. R. 1991, ApJ, 379, 245
Savage, B. D., Bohlin, R. C., Drake, J. F., & Budich, W. 1977, ApJ, 216, 291
Schaye, J. 2001, ApJ, 562, L95
Shaw, G., Ferland, G. J., Abel, N. P., Stancil, P. C., & van Hoof, P. A. M. 2005, ApJ, 624, 794
Silva, A. I., & Viegas, S. M. 2002, MNRAS, 329, 135
Snow, T. P., & McCall, B. J. 2006, ARA&A, 44, 367
Sonnentrucker, P., Friedman, S. D., Welty, D. E., York, D. G., & Snow, T. P. 2002, ApJ, 576, 241
Srianand, R., & Petitjean, P. 2000, A&A, 357, 414
Srianand, R., Petitjean, P., Ledoux, C., Ferland, G., & Shaw, G. 2005, MNRAS, 362, 549
Srianand, R., Noterdaeme, P., Ledoux, C., & Petitjean, P. 2008, A&A, 482, L39
Srianand, R., Rahmani, H., Muzahid, S., & Mohan, V. 2014, MNRAS, 443, 3318
Tripp, T. M., Lu, L., & Savage, B. D. 1998, ApJ, 508, 200
Tumlinson, J., Shull, J. M., Rachford, B. L., et al. 2002, ApJ, 566, 857
Vreeswijk, P. M., Ellison, S. L., Ledoux, C., et al. 2004, A&A, 419, 927
Wagenblast, R. 1992, MNRAS, 259, 155
Welty, D. E., Lauroesch, J. T., Blades, J. C., Hobbs, L. M., & York, D. G. 1997, ApJ, 489, 672
Welty, D. E., Hobbs, L. M., & Morton, D. C. 2003, ApJS, 147, 61
Welty, D. E., Xue, R., & Wong, T. 2012, ApJ, 745, 173
Wolfe, A. M., Turnshek, D. A., Smith, H. E., & Cohen, R. D. 1986, ApJS, 61, 249
Wolfe, A. M., Prochaska, J. X., & Gawiser, E. 2003, ApJ, 593, 215
Wolfe, A. M., Howk, J. C., Gawiser, E., Prochaska, J. X., & Lopez, S. 2004, ApJ, 615, 625
Wolfe, A. M., Gawiser, E., & Prochaska, J. X. 2005, ARA&A, 43, 861
York, D. G., Adelman, J., Anderson, J. E. Jr., et al. 2000, AJ, 120, 1579
Zafar, T., Centurión, M., Péroux, C., et al. 2014, MNRAS, 444, 744
Zwaan, M. A., & Prochaska, J. X. 2006, ApJ, 643, 675